AIAA JOURNAL
Vol. 39, No. 5, May 2001

Wave Computation in Compressible Flow Using Space–Time Conservation Element and Solution Element Method

Ching Y. Loh,* Lennart S. Hultgren,† and Sin-Chung Chang‡
NASA John H. Glenn Research Center at Lewis Field, Cleveland, Ohio 44135

The recently developed space–time conservation element solution element method has several attractive features for aeroacoustic computations. The scheme is robust, possesses almost no dispersion error, and the implementation of nonreflecting boundary conditions is simple and effective. The scheme is tested for several problems ranging from linear acoustic waves to strongly nonlinear phenomena, with special emphasis on mixing-layer instability, and good numerical results are achieved.

I. Introduction

In recent years, a conceptually new numerical method for fluid dynamics computation (CFD) has been developed by Chang and his collaborators.[1–8] The method is termed the space–time conservation element and solution element (CE/SE) method. It is distinguished by the simplicity of its conceptual basis: flux conservation in both space and time. The CE/SE method is different in nature from previous numerical methods. In a nutshell, it systematically solves a set of integral equations derived directly from the physical conservation laws. A detailed description and comparison to conventional finite volume upwind methods may be found in Refs. 8 and 7, respectively. The development of the method was primarily guided by the following requirements/ideas: 1) To enforce both local and global flux conservation in space and time, space and time are unified and treated on the same footing. 2) Fluxes are truly multidimensional and directly evaluated at the interfaces (solution elements) of immediately neighboring cells, with no interpolation and no dimensional splitting. 3) Both dependent flow variables and their derivatives are solved for simultaneously; however, there is no need to extend the computations to a stencil of cells to achieve this.

As has been shown in a series of papers and reports,[1–8] the CE/SE method is robust enough to cover the complete spectrum of inviscid flow from linear acoustic waves all of the way to high-speed flows with shocks. In this paper, several select two-dimensional benchmark problems, spanning the whole specified range are considered, to further establish CE/SE as a viable tool for computational aeroacoustics (CAA). The scheme is used in 1) solving a benchmark linear CAA problem, 2) computing instability waves on a two-dimensional compressible free shear layer, which is an important problem closely related to jet-noise prediction, and 3) simulating vortex–shock interactions. Both cases 2 and 3 involve nonlinear effects. The behavior of the CE/SE scheme is illustrated in each example.

Several higher-order compact methods have been employed in the past by others to solve problems 1 and 2 and have yielded excellent results, for example, Refs. 9–11. It is not the purpose of this paper to claim that the CE/SE method would necessarily be superior to such methods for a particular application such as these two test cases, but rather to show that the method is capable of solving these types of problems effectively and accurately, which we believe is a prerequisite for CAA computation. The great strength of the CE/SE method is that it is a very robust, intrinsically shock-capturing scheme and has no difficulty in dealing with vortex–shock interactions. Therefore, it can be expected to deal effectively with a variety of important and real-world CAA problems (nonlinear or linear).

The paper is arranged as follows. The two-dimensional CE/SE scheme is briefly discussed in Sec. II. In particular, the novel nonreflecting boundary conditions, which are based on flux balance rather than the conventional theory of characteristics for differential equations, are illustrated. Section III describes the test cases and their numerical solution, with particular emphasis put on the shear-layer instability problem. In Sec. IV, the conclusion is drawn that the CE/SE method is a valuable tool for CAA and hybrid CAA/CFD computations.

II. Two-Dimensional CE/SE Euler Method

In this section, a prototype of the CE/SE method for the two-dimensional Euler equations is outlined. A detailed description of the two-dimensional CE/SE approach may be found in Refs. 7 and 8.

A. Conservation Form of the Two-Dimensional Unsteady Euler Equations

Consider a dimensionless conservation form of the Euler equations of a perfect gas. Let ρ, u, v, p, and γ be the density, streamwise velocity component, transverse velocity component, static pressure, and constant specific heat ratio, respectively. Then, the two-dimensional unsteady Euler equations can be written in the following vector form:

$$\boldsymbol{U}_t + \boldsymbol{F}_x + \boldsymbol{G}_y = 0 \tag{1}$$

where x, y, and t are the streamwise and transverse coordinates and time, respectively, and the conservative flow variable vector $\boldsymbol{U} = (U_1, U_2, U_3, U_4)^T$, with

$$U_1 = \rho, \qquad U_2 = \rho u, \qquad U_3 = \rho v$$

$$U_4 = p/(\gamma - 1) + \rho(u^2 + v^2)/2$$

and the corresponding flux vectors in the streamwise and transverse directions, $\boldsymbol{F}$ and $\boldsymbol{G}$, are given in Ref. 8. Moreover, due to the property of the Euler equations, $\boldsymbol{F}$ and $\boldsymbol{G}$ are homogeneous functions of degree 1, and hence,

$$\boldsymbol{F} = \frac{\partial \boldsymbol{F}}{\partial \boldsymbol{U}}\boldsymbol{U}, \qquad \boldsymbol{G} = \frac{\partial \boldsymbol{G}}{\partial \boldsymbol{U}}\boldsymbol{U} \tag{2}$$

When x, y, and t are considered as coordinates of a three-dimensional Euclidean space E_3 and when the Gauss' divergence theorem is used, it follows that Eq. (1) is equivalent to the following integral conservation laws:

$$\oint_{S(V)} \boldsymbol{H}_m \cdot \mathrm{d}\boldsymbol{S} = 0, \qquad m = 1, 2, 3, 4 \tag{3}$$

where $S(V)$ is the boundary of an arbitrary space–time region V in E_3 and $\boldsymbol{H}_m = (F_m, G_m, U_m)$.

Presented as Paper 98-0369 at the AIAA 36th Aerospace Sciences Meeting, Reno, NV, 11–14 January 1998; received 27 July 1999; revision received 14 August 2000; accepted for publication 27 September 2000.

*Research Scientist, Taitech, Inc., Member AIAA.
†Senior Scientist, Turbomachinery and Propulsion Systems Division. Associate Fellow AIAA.
‡Senior Scientist, Turbomachinery and Propulsion Systems Division. Member AIAA.

B. CE/SE Structure

In the CE/SE scheme, the flux conservation relation in space–time is the only mechanisms that transfers information between node points. The conservation element (CE), or computational cell, is the finite volume to which the integral flux condition (3) is to be applied and is similar to a control volume in the finite volume method. Discontinuities are allowed to occur in the interior of a conservation element. A solution element (SE) associated with a grid node is here a set of three interface planes in E_3 that passes through this node. In contrast to the conventional finite volume schemes, not only $\boldsymbol{U}$ but also its derivatives $\boldsymbol{U}_x$ and $\boldsymbol{U}_y$ are defined as a set of unknowns and solved for at these nodes. Within a given solution element SE(j, k, n), where (j, k, n) is the node index, the flow variables are not only considered continuous but are also approximated by linear Taylor expansions in E_3, that is, in both space and time (see Ref. 8). Partial derivatives of $\boldsymbol{F}$ and $\boldsymbol{G}$ in these expansions can be related to the corresponding one of $\boldsymbol{U}$ by using the chain rule and $\boldsymbol{U}_t$ can be obtained from Eq. (1). The discrete approximation of Eq. (3) is then

$$\oint_{S(\mathrm{CE})} \boldsymbol{H}_m^* \cdot \mathrm{d}\mathbf{S} = 0, \qquad m = 1, 2, 3, 4 \tag{4}$$

where $\boldsymbol{H}_m^* = (F_m^*, G_m^*, U_m^*)$. Each $S(\mathrm{CE})$ is made up by surface segments belonging to two neighboring SEs. All of the unknowns are solved for based on these relations. No extrapolations (interpolations) across a stencil of cells are needed. Conceptually, the physical conservation laws are strictly followed.

So that the number of equations derived from the stated flux conservation law matches the number of unknowns (here 12 scalar unknowns), the grid needs to be carefully designed.[1,8] In the following, a mesh that proves to work well with the CE/SE scheme is shown. The mesh is staggered in both time and space. In a spatial plane in E_3, the grid nodes (Fig. 1) are grouped as two staggered sets Ω_1 (open circles) and Ω_2 (filled circles). At a given time step, the unknowns are evaluated only on one of the grid sets, Ω_1 or Ω_2, and at the next time step it will be evaluated on the other set, that is, the spatial sets alternate as time is stepped forward. Within each of the two sets, Ω_1 and Ω_2, the grid points are staggered by the amount $(\Delta x, \frac{1}{2}\Delta y)$, where $2\Delta x$ and Δy are the grid increments for fixed y and fixed x, respectively. The grid set Ω_2 is shifted the amount $\frac{2}{3}\Delta x$ in x with respect to Ω_1. As can be seen in Fig. 1, each interior node point then has three nearest neighbors at the previous half-time step, $t - \frac{1}{2}\Delta t$, with Δt denoting the time increment for grid points belonging to either Ω_1 or Ω_2. Thus, there are three CEs associated with each node point in this arrangement and, therefore, there are the same number of relations as there are unknowns. Figure 2 shows the three conservation elements associated with a node point (solid circle) and its three nearest neighbors (open circles) at the previous time step. Because of the staggered spatial grids, the method can be thought of as a two-step method in time.

The reader is referred to Ref. 8 for full details of the implementation of the two-dimensional CE/SE Euler method leading to the a, a-ϵ, and weighted a-ϵ schemes. The ϵ is an adjustable parameter that controls the numerical dissipation added to the basic nondissipative CE/SE a scheme, and the weighted scheme is intended for cases where discontinuities may be present in the inviscid flowfield. The weighted a-ϵ scheme is used in the present study.

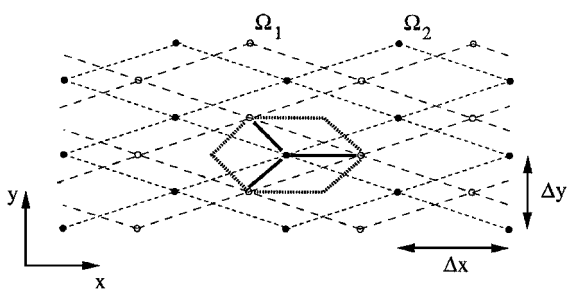

Fig. 1 Double staggered grid in E_3.

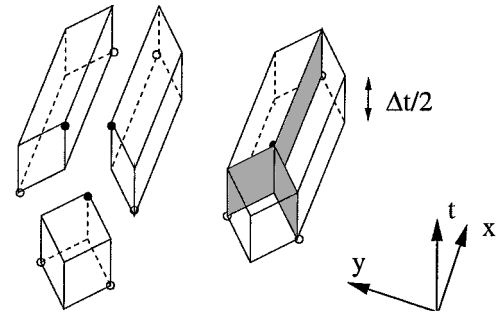

Fig. 2 Three CEs (or control volumes) associated with a grid point at the current time (•).

C. Nonreflecting Boundary Conditions

The nonreflecting boundary condition plays an important role in CAA and computational fluid dynamics. Without a sufficiently effective nonreflecting boundary condition, reflected signals will inevitably contaminate the computed flowfield or lead to a heavy CPU time consumption before final or sufficient convergence is achieved. Theoretical analysis and numerical practice of the nonreflecting boundary condition have been a research topic for a long time, for example, Refs. 9–18. Generally speaking, most of these techniques are based on a fundamental result in partial differential equation theory, namely, that signals propagate along characteristics. If one can stop the signal from reflecting back along a characteristic, the boundary condition will be nonreflecting. In the current literature, generally there are three methods to implement a nonreflecting boundary conditions. They are as follows.

The first method is the use of one-dimensional characteristic variables (Riemann invariants) in the normal direction of the boundary. Engquist and Majda[13] express the nonreflecting boundary condition as the requirement that the local perturbation propagated along incoming characteristics be made to vanish. In practice, this consists of projecting the equations onto the normal direction of the boundary, converting the conservative variables to characteristic variables, finding the characteristics that enter the domain, and finally setting the corresponding characteristic variable to zero. Although such a procedure is delicate and tedious, it is still the most popular boundary treatment among most of the CAA schemes.[9,10,12–16]

The second method is minimization of the reflections from the boundaries by inserting a buffer zone between the core computational domain and the boundary; for example, see Refs. 10 and 16. The most recent development in this area is the so-called perfectly matched layer (PML) method[17,18]

The third method is the use of an asymptotic analytical solution at the far-field boundary.[11]

In the CE/SE scheme, the idea of characteristics stemming from differential equation theory does not properly apply because a set of integral equations instead of differential equations are being solved. For the nonreflecting boundary condition for the CE/SE scheme, the following basic criterion is adopted: In a CE (or generalized CE[5]) located at the numerical domain boundary, a nonreflecting boundary condition is equivalent to letting the incoming flux from the interior domain to the boundary CE smoothly exit to the exterior of the domain.

This principle is conceptually different from that of the method of characteristics and is much simpler to implement. Chang et al.[5] have detailed discussions and examples of various implementations of this criterion for the one-dimensional case. It was demonstrated in their paper that only negligible reflection occurs even when a shock passes through a boundary with this type of flux-based condition.

It is believed that the same basic principle for implementing a nonreflecting boundary conditions for the CE/SE scheme carries over to the two-dimensional (or even higher dimension) case. As a matter of fact, the two-dimensional nonreflecting boundary conditions described here have been successfully applied to CAA computations for a while.[2–6] There are various versions of the nonreflecting boundary condition and the following are typical ones employed

in our computations. For a grid node (j, k, n) lying at the domain boundary, the first one, labeled type I, requires that

$$(\boldsymbol{U}_x)^n_{j,k} = (\boldsymbol{U}_y)^n_{j,k} = 0$$

while $\boldsymbol{U}^n_{j,k}$ is kept fixed at the initially given steady boundary value. Type II, for cases where there is a substantial gradient in, for example, the y direction, requires that

$$(\boldsymbol{U}_x)^n_{j,k} = 0$$

while $\boldsymbol{U}^n_{j,k}$ and $(\boldsymbol{U}_y)^n_{j,k}$ are now defined by simple extrapolation from the interior, that is,

$$\boldsymbol{U}^n_{j,k} = \boldsymbol{U}^{n-\frac{1}{2}}_{j',k'}, \qquad (\boldsymbol{U}_y)^n_{j,k} = (\boldsymbol{U}_y)^{n-\frac{1}{2}}_{j',k'}$$

The proposed nonreflecting boundary conditions are all simple, truly multidimensional, and effective. Our experiences show that, in general, the reflection amounts to about 1%. For boundaries with an abrupt change, for example, a shock passing through, the reflection is somewhat higher.

III. Two-Dimensional Numerical Test Problems

The two-dimensional CE/SE Euler scheme is tested to demonstrate its capability and robustness for aeroacoustics computations. Several selected benchmark problems in linear aeroacoustics as well as nonlinear aeroacoustics computations are considered. The numerical results, which cover a wide spectrum of waves, from linear and nonlinear acoustic waves to discontinuous waves (shocks), are then compared to available exact solutions. The behavior of the CE/SE scheme is illustrated in each example.

A. Acoustic Pulse, Entropy Wave, and Vorticity Wave Propagation

For the two-dimensional aeroacoustics computations, we begin with the benchmark problem on linear acoustic waves from the NASA Langley Research Center CAA Workshop[19] (category 3, problem 1). The computational domain in the x–y plane is a rectangular one with $-100 \le x \le 100$ and $-100 \le y \le 100$. A uniform 200×200 grid is used with $\Delta x = \Delta y = 1$, cf. Fig. 1. Initially, a Gaussian acoustic pulse is located at the center of the domain $(x = y = 0)$, and a weaker entropy/vorticity disturbance is located off center $(x = 67,\ y = 0)$. The uniform background mean flow is in the x direction with Mach number $M = 0.5$. After appropriate nondimensionalization, the corresponding pressure, density, and streamwise and transverse velocity components are given by

$$p = (1/\gamma) + \delta \exp\left[-\alpha_1(x^2 + y^2)\right]$$

$$\rho = 1 + \delta\left(\exp\left[-\alpha_1(x^2 + y^2)\right] + 0.1\exp\left\{-\alpha_2[(x - 67)^2 + y^2]\right\}\right)$$

$$u = M + 0.04\delta y \exp\left\{-\alpha_2[(x - 67)^2 + y^2]\right\}$$

$$v = -0.04\delta(x - 67)\exp\left\{-\alpha_2[(x - 67)^2 + y^2]\right\}$$

where $\alpha_1 = \ell n\frac{2}{9}$, $\alpha_2 = \ell n\frac{2}{25}$, and δ is an amplitude factor. All of the conditions are set exactly the same as in the workshop benchmark problem (this includes the number of spatial grid points used) except for the amplitude factor δ. In the CAA workshop, the problem was solved based on linearized Euler equations, and the amplitude factor can be chosen as unity. Because the CE/SE scheme is based on the fully nonlinear Euler equations, linearization is achieved by choosing a small amplitude for the acoustic waves. For example, one may choose $\delta = 0.001$ as is done here. As is well known, for example, Refs. 11 and 19, the two-dimensional linearized Euler equations support three types of waves, namely, pressure, entropy, and vorticity waves. For the present problem, the exact solutions can be expressed in terms of Bessel functions.[19] These exact solutions will be used to compare with our numerical results.

A large Δt [large Courant–Friedrichs–Lewy (CFL) number] and a small ϵ are suggested for aeroacoustics computation to reduce numerical damping as much as possible in the CE/SE scheme. $\Delta t = 0.6$ (corresponding to CFL = 0.91) and $\epsilon = 0.1$ were used in this example. This time step is comparable to those used by others in Ref. 19.

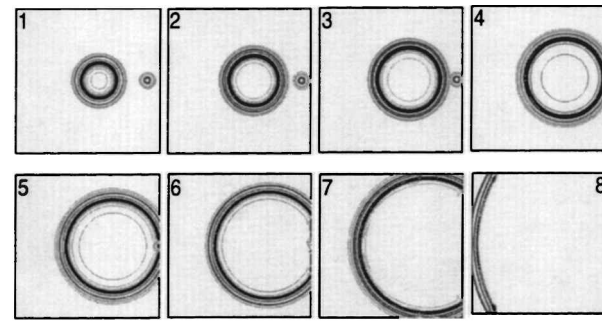

isopycnics at t=30,40,50,60,70,80,100 and 200 (Cat.3.1)

a) Constant density contours

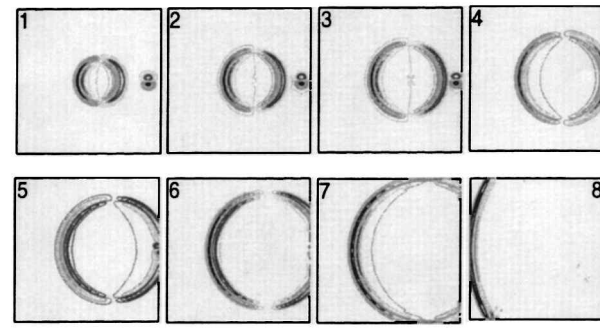

u- contours at t=30,40,50,60,70,80,100 and 200 (Cat.3.1)

b) Constant u-velocity contours

Fig. 3 Propagation of an acoustic pulse and a vorticity/entropy disturbance.

In addition, with the absence of flow discontinuity, the weighted average index α in the CE/SE scheme is set to zero to avoid any excessive numerical dissipation.

During the computation, the nonreflecting boundary condition of the described type I is enforced at all of the four sides of the computational domain. Generally speaking, if the reflection coefficient C_r is defined as $C_r = (f_{\text{numerical}} - f_{\text{exact}})/f_{\max}$, where f is any perturbed flow variable such as pressure, density, etc., the preceding simple nonreflecting boundary conditions render a C_r in the range of about 1%, which is comparable to any of the characteristic-type nonreflecting boundary conditions commonly used for conventional finite difference or finite volume schemes. Figure 3 shows the isopycnics (density) contours and u-velocity contours at $t = 30$, 40, 50, 60, 70, 80, 100, and 200 in eight frames. The acoustic-pulse ring is clearly displayed; it propagates in all directions with the speed of sound, while being convected downstream by the mean flow. Figure 3 also demonstrates that the entropy and vorticity disturbances, that is, the nonacoustic ones, are convected downstream by the mean flow while essentially remaining intact. Figure 3 shows that the simple nonreflecting boundary condition is effective; practically no reflection is observed when the (pressure, entropy, and vorticity) waves cross the domain boundaries. The worst situation occurs in the vicinity of the domain corners. Figure 4 shows the comparison of perturbed density distributions along the domain horizontal centerline with the exact solutions at $t = 60$ and 100, respectively. It is seen that the numerical results agree well with the theoretical ones. No visible dispersion error or numerical reflection at the exit boundary is observed.

B. Free Shear-Layer Instability

In the next two examples, using the CE/SE Euler scheme, we study the inviscid linear and nonlinear instability properties of a free shear layer. This important class of flows forms the basis of jet noise generation theory and has been the subject of many detailed analytical and experimental studies.

The direct numerical computation of the shear-layer instability is compared with linear results obtained using the normal mode approach. The background mean flow consists of a fast stream on the

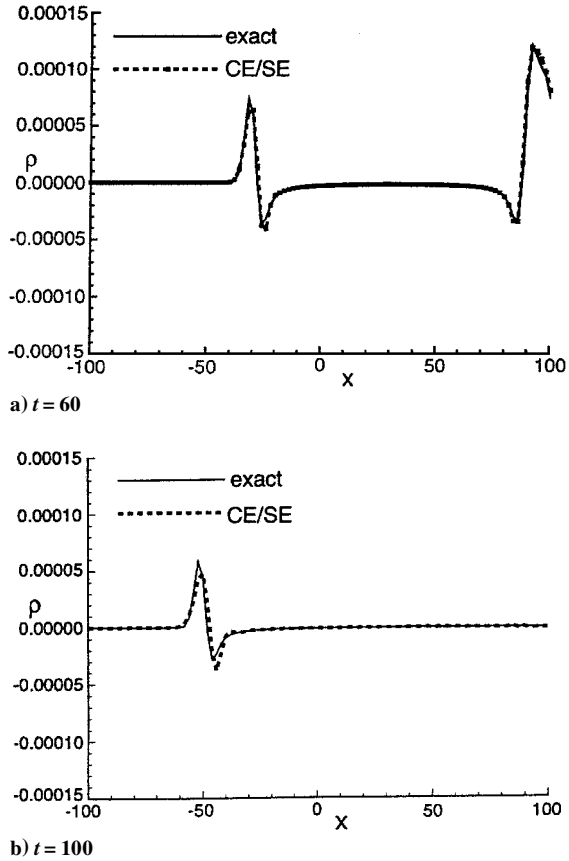

Fig. 4 Perturbation density along $y = 0$.

top half-domain and a slow stream at the bottom half, with the two parallel streams connected by a continuously changing shear layer. The streamwise velocity, density, and pressure in the fast stream are taken as velocity, density, and pressure scales, respectively, for the nondimensionalization. The length scale is taken as $\delta/2$, where δ is the vorticity thickness and is defined as

$$\delta = (U_{1*} - U_{2*}) \Big/ \left(\frac{\mathrm{d}U_*}{\mathrm{d}y_*}\right)_{\max}$$

with the subscript $*$ here denoting dimensional quantities. In a parallel flow, the mean pressure is constant, and the mean transverse velocity vanishes all over the domain, whereas the mean streamwise velocity and density profiles must be specified.

In the linear stability theory, the normal mode assumption is made, that is,

$$\phi(x, y, t) = \hat{\phi}(y) \exp[i(\alpha x - \omega t)] \tag{5}$$

where $\phi(x, y, t)$ are the perturbation velocities u', v', pressure p', or density ρ' and α and ω are the complex wave number and real angular frequency of the disturbance, respectively. We note that $\hat{u}$, $\hat{v}$, $\hat{p}$, and $\hat{\rho}$ are also complex functions in general. When the preceding perturbations are added to the corresponding mean flow variables and substituted into the two-dimensional Euler equations, a set of equations for the unknown perturbation flow variables is obtained. Assume that the mean flow variables satisfy the Euler equations and eliminate those terms of second order or higher, then the compressible Rayleigh equation in terms of the perturbation pressure eigenfunction component $\hat{p}$ can be achieved after some manipulation:

$$\frac{\mathrm{d}^2\hat{p}}{\mathrm{d}y^2} - \left(\frac{2U'}{U-c} - \frac{T'}{T}\right)\frac{\mathrm{d}\hat{p}}{\mathrm{d}y} - \alpha^2\left[1 - \frac{M_1^2}{T}(U-c)^2\right]\hat{p} = 0 \tag{6}$$

where the prime now represents derivatives with respect to y, M_1 is the Mach number of the fast flow, U and T are the mean flow streamwise velocity and temperature, and $c = \omega/\alpha$. The use of the temperature T is simply a matter of convenience; it can be deduced from the mean flow pressure and density.

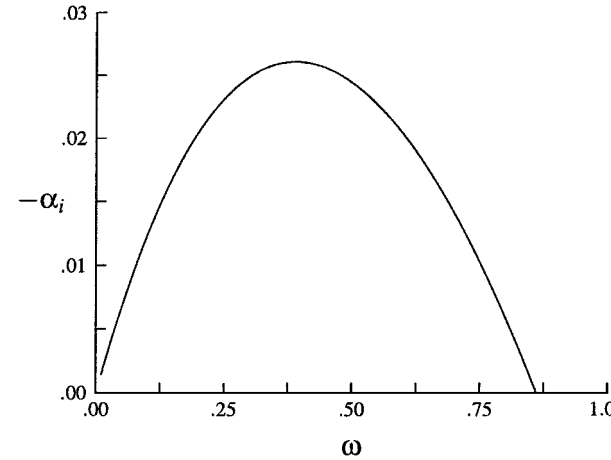

Fig. 5 Spatial growth rate; $-\alpha_i$ vs angular frequency ω for linear shear-layer perturbations.

To be specific, the streamwise mean flow velocity U is here taken as

$$U(y) = \frac{1 + R\tanh y}{1 + R} \tag{7}$$

where R is the velocity ratio of the shear layer. We further assume for simplicity that the Prandtl number is unity and the mean flow temperature T distribution is then obtained from the Buseman–Crocco relation:

$$T = T_2 + [(1 - T_2)/(1 - U_2)](U - U_2) + \tfrac{1}{2}(\gamma - 1) \times M_1^2(U - U_2)(1 - U) \tag{8}$$

where the subscripts 1 and 2 are the fast stream and slow stream variables, respectively. T in turn yields the density distribution across the shear layer. As in Ref. 9, we choose the parameters

$$R = 0.15, \qquad M_1 = 1.5, \qquad T_2 = 1.85$$

Then the nondimensional flow states are worked out as

$$U_1 = 1, \qquad V_1 = 0, \qquad p_1 = 1/3.15$$
$$T_1 = 1, \qquad \rho_1 = 1, \qquad M_1 = 1.5$$
$$U_2 = 0.7391304, \qquad V_2 = 0, \qquad p_2 = 1/3.15$$
$$T_2 = 1.85, \qquad \rho_2 = 0.5405405$$

Under the preceding conditions, with an appropriate ω chosen, the complex eigenfunction component $\hat{p} = \hat{p}_r + i\hat{p}_i$ and the corresponding eigenvalue $\alpha = \alpha_r + i\alpha_i$, where the subscripts r and i are real and imaginary parts, respectively, can be found by solving the compressible Rayleigh equation (6). The solution procedure consists of a shooting method utilizing an Adam–Bashforth predictor-corrector scheme. Once $\hat{p}$ is computed, the other eigenfunction components $\hat{u}$, $\hat{v}$, and $\hat{\rho}$ can be obtained through simple algebraic or differential relations. Figure 5 shows the relation between ω and $-\alpha_i$, the latter of which is the spatial (exponential) growth rate of the disturbance. In the test, we shall choose the value of ω that corresponds to the maximum growth rate (most unstable).

In the test examples to follow, the computational domain spans between $0 \le x \le 300$ and $-10 \le y \le 10$, with a grid of 601×101, respectively, that is, $\Delta x = 0.5$ and $\Delta y = 0.2$ in Fig. 1. To reduce the numerical damping as much as possible, the time step size $\Delta t = 0.15$, $\epsilon = 0.2$, and the weighted average index $\alpha = 0$ were found appropriate. The computation of the unsteady flow is carried out until $t = 390$ ensuring that the spatial instability is fully developed.

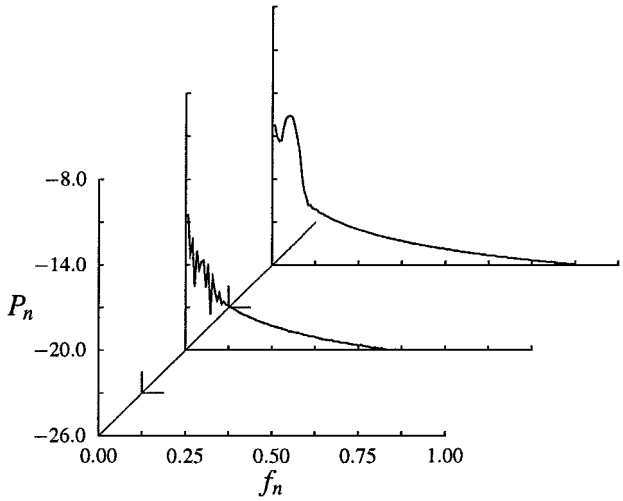

Fig. 6 Power spectra at $x = 150$ and 250 for natural (unforced) case; coarse grid.

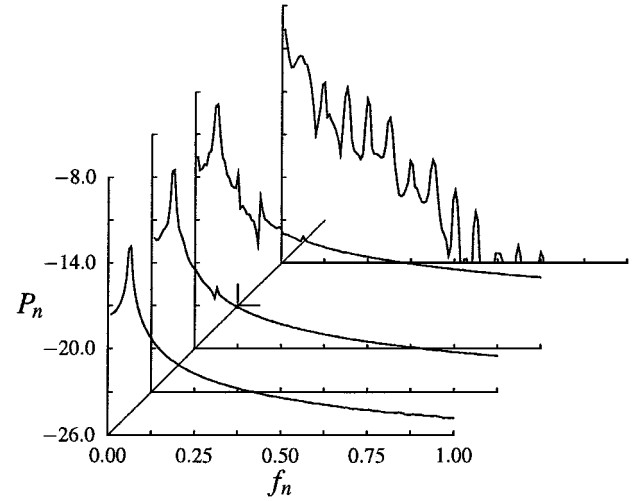

Fig. 7 Power spectra at $x = 050$, 100, 150, and 250 with forcing at the most unstable frequency according to linear theory; coarse grid.

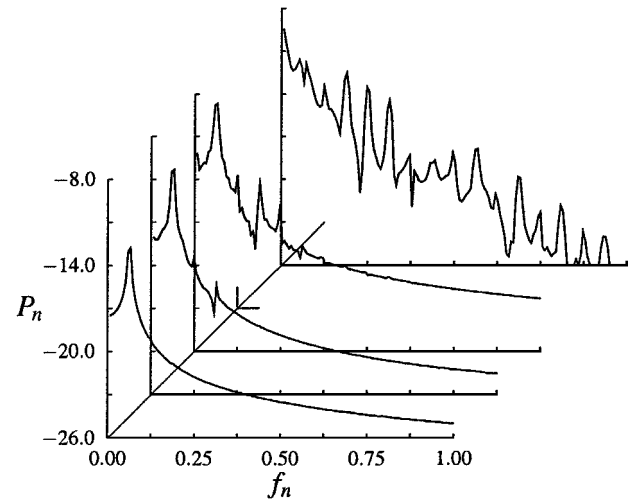

Fig. 8 Power spectra at $x = 050$, 100, 150, and 250 with forcing at most unstable frequency according to linear theory; finer grid.

1. Inherent Instability of a Free Shear Layer

In our first example, no disturbance is imposed on the shear layer. Nonreflecting type-I boundary conditions are imposed at the top and bottom of the computational domain and a nonreflecting type-II boundary condition is imposed at the downstream boundary because there is a strong mean flow gradient parallel to that boundary. The initial conditions for the computation is that the flow equals the prescribed mean flow everywhere. Because there is no disturbance, the inflow boundary condition is exactly the same as the initial condition. Ideally, in the absence of any forcing, the flowfield should remain at its original value for all times. However, although no disturbance is intentionally imposed on or introduced into the flow, the shear layer is in reality continuously stimulated at a very low level as a result of truncation, roundoff, and discretization errors (numerical noise). Among these tiny excitations, those whose frequency falls within the unstable frequency range (see Fig. 5) will grow and all others will eventually decay out. From Fig. 5, it can be seen that the unstable (nondimensional) angular frequency range, for the parameters under consideration here, is $0 < \omega < 0.86$ or $0 < f < 0.137$, where $f = \omega/2\pi$ is a nondimensional frequency. The maximum growth occurs for $\omega = 0.39$ or $f = 0.062$. Figure 6 shows the power spectrum P_n of the computed streamwise perturbation velocity component u' in natural log scales at the stations $x = 150$ and 250 vs the normalized frequency f_n. It is observed in Fig. 6 that disturbances amplify within the unstable frequency range given by linear stability theory, that is, the shear layer is a select amplifier, with the resulting broad peak in the spectra centered about the most unstable frequency.

2. Linear, Nonlinear Instability of a Free Shear Layer and Vortex Rollup

In studying the instability of a free shear layer and the consequent vortex rollup and noise generation, one is mainly interested in the most unstable mode that dominates the nonlinear vortex rollup. To investigate such instabilities, from now on we shall enforce a small harmonic perturbation at a single frequency at the inlet boundary and compute the resulting development of the spatial instability wave.

From the chart of ω vs $-\alpha_i$ (Fig. 5), it can be observed that the exponential growth rate $-\alpha_i$ reaches its maximum of about 0.026 when the angular frequency $\omega = 0.39$, and the latter is the value used in the following test example. The complex spatial eigenvalue $\alpha = 0.43693 - 0.02607i$ and the corresponding eigenmode is then determined by solving the compressible Rayleigh equation (6) for this value of ω. The eigenfunction is normalized such that the maximum rms value of the streamwise velocity component is unity. The forcing at the inlet boundary ($x = 0$) then has the form

$$\phi = \delta[\hat{\phi}_r \cos\omega t + \hat{\phi}_i \sin\omega t] \tag{9}$$

$$\frac{\partial\phi}{\partial x} = \delta[-(\hat{\phi}_r\alpha_i + \hat{\phi}_i\alpha_r)\cos\omega t - (\hat{\phi}_i\alpha_i - \hat{\phi}_r\alpha_r)\sin\omega t] \tag{10}$$

$$\frac{\partial\phi}{\partial y} = \delta[\hat{\phi}'_r \cos\omega t + \hat{\phi}'_i \sin\omega t] \tag{11}$$

where ϕ is any of the eigenfunction components u', v', p', or ρ', and δ is the forcing amplitude. To fully demonstrate the capability of the CE/SE scheme to compute both linear and nonlinear instability waves, the forcing amplitude δ is taken to be $1/1000$.

Figure 7 shows the power spectrum P_n of the computed u' in natural log scale at the streamwise stations $x = 50$, 100, 150, and 250, which correspond to about 3.5, 7 wavelengths, and so on. At $x = 50$, there is a clearly discernable peak centered about the forcing frequency $f = 0.062$. At about $x = 100$, second and third harmonics start to emerge. Farther downstream, more harmonics appear, and eventually the fundamental saturates. To assess the grid dependence of the numerical results, the computation was repeated with half-grid sizes and time step size. The corresponding power spectra is shown in Fig. 8. Comparing Figs. 7 and 8 shows that they are quite similar except that, as expected, the finer grid allows higher harmonics to be better resolved.

The streamwise evolution of the disturbance amplitude along the horizontal centerline $y = 0$ is shown in Fig. 9. Numerical results for both the coarse and finer grids are presented and compared to the theoretical linear growth. It is seen that for $0 \le x \le 100$ (about 7 wavelengths) the coarse-grid and fine-grid computations yield good agreement both between themselves and with the linear result. Farther downstream, nonlinear effects become important, the growth rate is reduced from the linear value, and ultimately the fundamental

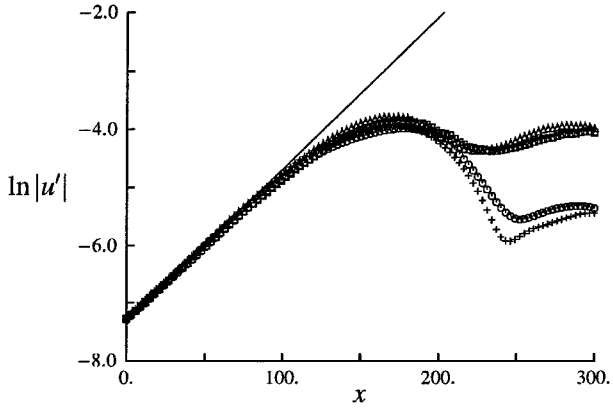

Fig. 9 Streamwise evolution of disturbance amplitude with forcing at the most unstable frequency according to linear theory: □, total u_{rms}, coarse grid; △, total u_{rms}, finer grid; ○, u_{rms} at forcing frequency, coarse grid; ×, u_{rms} at forcing frequency, finer grid; and ——, linear growth.

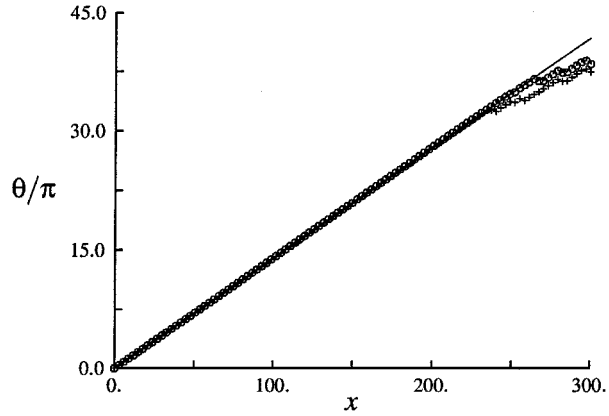

Fig. 10 Streamwise evolution of disturbance phase with forcing at the most unstable frequency according to linear theory: ○, coarse grid; ×, finer grid; and ——, linear result.

saturates. Both numerical results also agree reasonably well with each other in this nonlinear region. As the fundamental wave continues to roll up, the deviation between the results for the two grids becomes larger indicating that further grid refinement is needed in this region. However, the qualitative behavior of the curves are the same even here. The computations show that the results are, in general, grid independent, but with some room for further improvement in the later part of the nonlinear stage.

Figure 10 shows the streamwise evolution of the disturbance phase. The numerical results for both the coarse and finer grids are compared to the corresponding result from linear theory. The agreement is surprisingly good until well into the nonlinear region. This means that even though the growth rate of the disturbance is reduced by nonlinear effects its wave length is essentially unaffected by the nonlinearity.

Figure 11 compares the normalized $|u'|$ profile across the shear-layer flow with the eigenfunction from linear stability theory at the streamwise station $x = 100$, which is located toward the end of the linear growth region. The agreement is excellent. The phase variation across the shear layer of the disturbance at the same station is shown in Fig. 12. Except for a small region at the top, the agreement is also very good here.

Figure 13 shows the vorticity contours from both the coarse and finer grids. Vortex rollup is clearly observed in Fig. 13. Both computations present almost identical results except that the finer-grid result, as expected, leads to a sharper image in the later stages. Figure 13 also shows isobars for the finer-grid computation. Figure 13 clearly demonstrates the effectiveness of the nonreflecting boundary conditions at the top, bottom, and outlet. We emphasize that the domain shown in the figures is exactly the computational domain, no buffer zones, cutoffs, or other numerical fixes are applied.

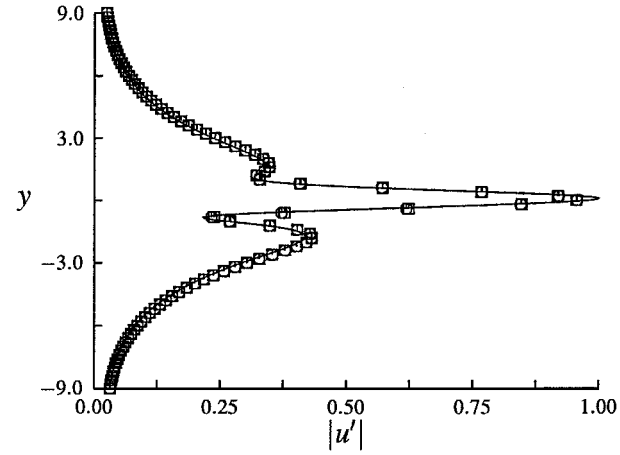

Fig. 11 Transverse mode shape at $x = 100$ with forcing at most unstable frequency according to linear theory, finer grid: □, total u_{rms}; ○, u_{rms} at forcing frequency; and ——, linear eigenfunction (modulus).

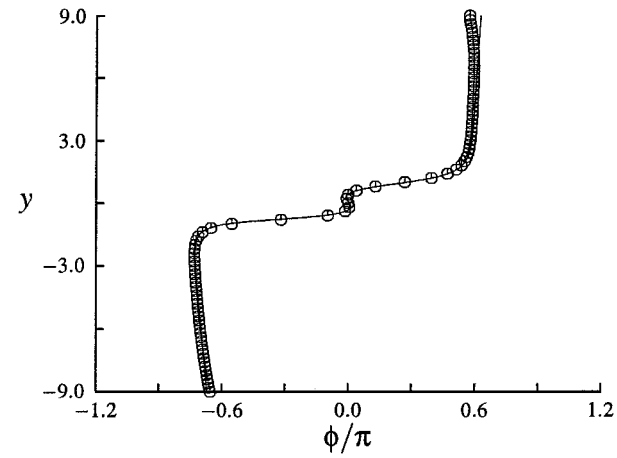

Fig. 12 Transverse phase variation at $x = 100$ with forcing at most unstable frequency according to linear theory, finer grid: ○, u_{rms} at forcing frequency, and ——, linear eigenfunction (phase).

C. Multiple Interaction of a Strong Vortex and Shocks

As a last numerical example, the multiple interaction of a strong vortex and oblique shocks is considered to illustrate that the CE/SE scheme is capable of handling highly nonlinear waves and complicated wave interactions. It is well-known that the interaction between a vortex and a shock may generate acoustic waves.[20–24] To our knowledge, most research on this topic, including both experimental and numerical computation, concentrates on a single interaction between a vortex and a normal shock. Results obtained by us using the CE/SE method for this simpler situation[24] qualitatively agree well with those obtained by other methods.[21,22] Yet only a modest 150×150 spatial grid was used in our CE/SE computation compared to the denser grids used by others, for example, 480×280 by Ellzay et al.[21] and 300×300 by Kao et al.[22]

A grid of 401×101 nodes is employed in the current problem with $\Delta x = \Delta y = 1$ (cf. Fig 1). The inflow boundary condition is given as a supersonic flow with a Mach number of 2.9:

$$u_0 = 2.9, \qquad v_0 = 0, \qquad p_0 = 1/1.4, \qquad \rho_0 = 1$$

The boundary condition at the top is an inclined flow:

$$u_t = 2.6193, \qquad v_t = -0.50632$$

$$p_t = 1.5282, \qquad \rho_t = 1.7000$$

The outflow boundary condition is the type-II nonreflecting one and the bottom is a solid reflecting wall. Then, a steady oblique shock is formed with 29-deg inclination and reflected at the bottom wall. The

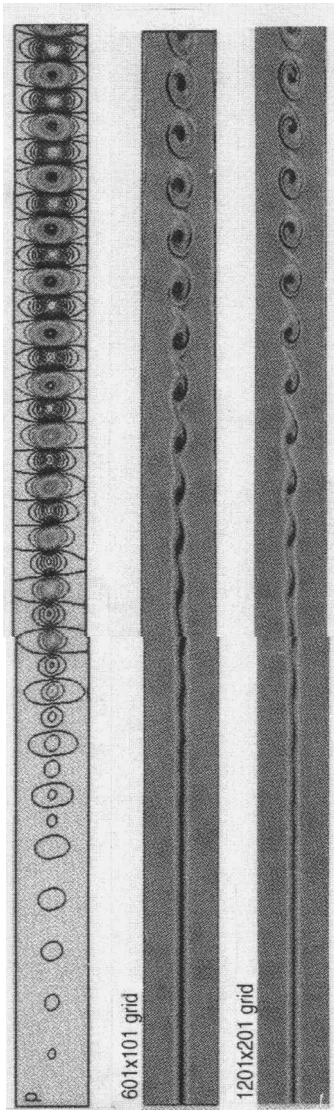

Fig. 13 Isobars (fine grid), vorticity contours for coarse and fine grids, all at $t = 390$.

flow with shocks is pre-calculated until a steady state is reached. It is then used as the background mean flow for further computation.

At $t = 0$, a strong Lamb's vortex is placed at $x = 22$ and $y = 60$. In a polar coordinates, the azimuthal and radial velocities of a Gaussian-type Lamb vortex are given as

$$u_\theta = -re^{-ar^2}, \qquad u_r = 0$$

respectively. In this case, the momentum and energy equations reduce to

$$\frac{\mathrm{d}p}{\mathrm{d}r} = \frac{\rho u_\theta^2}{r} \tag{12}$$

$$\frac{\gamma}{\gamma - 1}\frac{p}{\rho} + \frac{u_\theta^2}{2} = H_0 \tag{13}$$

where H_0 is a prescribed total enthalpy. When these two equations are combined, a differential equation for p is obtained that can be easily solved using numerical integration. Once this is accomplished, ρ and the entire stationary flowfield are also determined by using the preceding equations. The solution for this stationary vortex can then be superimposed on any uniform mean flow with a given streamwise velocity u_0.

In the numerical problem considered, u_θ and u_r are converted to

$$u = \delta y e^{-ar^2}, \qquad v = -\delta x e^{-ar^2}$$

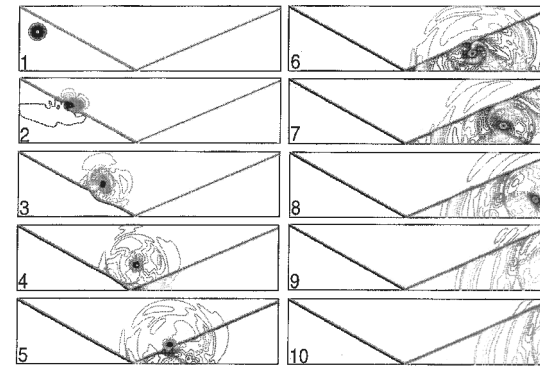

isobars for a vortex passing through shocks, with acoustic waves generated.

a) Isobars

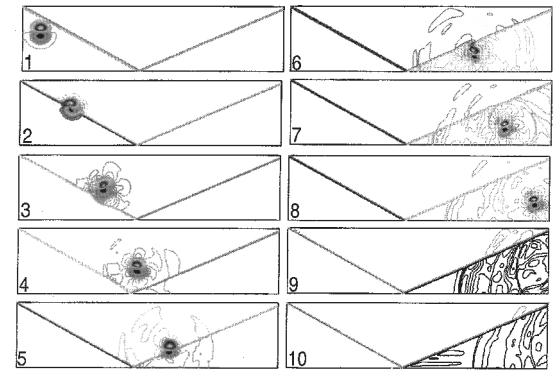

u-contours for a vortex passing through shocks

b) u-velocity contours

Fig. 14 Multiple interactions of a strong vortex and shocks producing nonlinear acoustic waves at $t = 2$, 20, 38, 56, 74, 92, 110, 128, 146, and 180.

where $\delta = 0.3$ is the chosen amplitude factor. As already discussed, p and ρ are functions of $r = [(x - u_0 t)^2 + y^2]^{1/2}$. This stationary vortex is, thus, superimposed on the background mean flow. The vortex is large and strong, because the pressure in the vortex center dips down to about 7% of its circumferential value. Because of the presence of shocks, the CE/SE scheme needs to have certain numerical damping. For this purpose, a weighted average index $\alpha = 2$ and $\epsilon = 0.5$ were chosen. The boundary conditions are the same as the oblique shocks computation. We chose $a = \ell n \frac{2}{784}$ and $\Delta t = 0.2$ and ran 900 time steps. Figure 14 demonstrates the shock–vortex interaction at the different times $t = 2$, 20, 38, 56, 74, 92, 110, 128, 146, and 180. The vortex propagates downstream while remaining intact before colliding with the oblique shock. As it propagates farther, it begins to interact with the first oblique shock (Fig. 14; plots 2 and 3). During the interaction, both the vortex and the shock are distorted. The straight oblique shock first changes to an S shape but then recovers its original straight-line shape. Figure 14, plot 2, shows how the collision disrupts the vortex. The ruptured vortex can no longer remain intact and begins to release its kinetic energy in the form of strong (nonlinear) acoustic waves (pressure amplitude is as high as 17% of the field maximum). The phenomenon is consistent with experiments and numerical computations for a normal shock–vortex interaction by other investigators.[20–24] In Fig. 14, plots 3 and 4, the disrupted eddy continues to emit acoustic waves. Some of the waves pass through the reflected shock and are reflected from the solid wall. In Fig. 14, plot 5, the weakening vortex is convected farther downstream and collides with the second oblique shock. It is then disrupted again and releases more energy in the form of acoustic waves. Figure 14 plots 6–8 show that more acoustic waves are emitted and that the vortex reduces its size (to about one-quarter of its original size) and its kinetic energy as well. Figure 14, plots 9 and 10 show the vortex propagating out from the computational domain along with the acoustic waves it generates, and the oblique shocks resume their original shapes.

IV. Conclusions

In the application of the recently developed CE/SE scheme to a select variety of typical, nontrivial, and relevant CAA problems, we have demonstrated the following attractive features of the approach.

1) The present (second-order) CE/SE scheme is efficient and yields high resolution, low dispersion results similar to those of higher-order conventional schemes.[9,11,16,19]

2) The novel nonreflecting boundary condition based on flux balance is easy to implement and removes the need for (or minimizes the size of) buffer zones.

3) The CE/SE scheme is capable of handling both continuous and discontinuous flows[1–8] and, thus, provides a unique numerical tool for flow situations where sound waves and shocks and their interactions are important such as the jet screech noise problem.

To optimize the numerical performance of the scheme, it is essential to choose a large CFL number and a small ϵ in any CAA computation.

References

[1]Chang, S. C., "The Method of Space–Time Conservation Element and Solution Element—A New Approach for Solving the Navier–Stokes and Euler Equations," *Journal of Computational Physics*. Vol. 119, 1995, pp. 295–324.

[2]Loh, C. Y., Chang, S. C., Scott, J. R., and Yu, S. T., "Application of the Method of Space–Time Conservation Element and Solution Element to Aeroacoustics Problems," 6th International Symposium on CFD, Lake Tahoe, NV, Sept. 1995.

[3]Loh, C. Y., Chang, S. C., Scott, J. R., and Yu, S. T., "The Space–Time Conservation Element Method—A New Numerical Scheme for Computational Aeroacoustics," AIAA Paper 96-0276, 1996.

[4]Loh, C. Y., Chang, S. C., and Scott, J. R., "Computational Aeroacoustics via the Space–Time Conservation Element/Solution Element Method," AIAA Paper 96-1687, 1996.

[5]Chang, S. C., Himansu, A., Loh, C. Y., Wang, X. Y., Yu, S.-T., and Jorgenson, P. C. E., "Robust and Simple Nonreflecting Boundary Conditions for the Space–Time Conservation Element and Solution Element Method," AIAA Paper 97-2077, 1997.

[6]Chang, S. C., Loh, C. Y., and Yu, S. T., "Computational Aeroacoustics via a New Global Conservation Scheme," *Proceedings of the 15th International Conference on Numerical Methods in Fluid Dynamics*, edited by P. Kutler, J. Flores, and J.-J. Chattot, Monterey, CA, June 1996.

[7]Chang, S. C., Yu, S. T., Himansu, A., Wang, X. Y., Chow, C. Y., and Loh, C. Y., "The Method of Space–Time Conservation Element and Solution Element—A New Paradigm for Numerical Solution of Conservation Laws," *Computational Fluid Dynamics Review*, edited by M. M. Hafez and K. Oshima, World Scientific, Singapore, 1998, pp. 206–240.

[8]Chang, S.-C., Wang, X.-Y., and Chow, C.-Y., "The Space–Time Conservation Element and Solution Element Method—A New High Resolution and Genuinely Multidimensional Paradigm for Solving Conservation Laws," *Journal of Computational Physics,* Vol. 156, 1999, pp. 89–136.

[9]Yu, S. T., Hultgren, L. S., and Liu, N. S., "Direct Calculations of Waves in Fluid Flows Using High Order Compact Difference Scheme," *AIAA Journal*, Vol. 32, No. 9, 1994, pp. 1766–1773.

[10]Colonius, T., Lele, S. K., and Moin, P., "Sound Generation in a Mixing Layer," *Journal of Fluid Mechanics*, Vol. 330, 1997, pp. 375–409.

[11]Tam, C. K. W., and Webb, J. C., "Dispersion-Relation-Preserving Finite Difference Scheme for Computational Acoustics," *Journal of Computational Physics*, Vol. 107, 1993, pp. 262–281.

[12]Gamet, L., and Estivalezes, J. L., "Nonreflexive Boundary Conditions Applied to Jet Aeroacoustics," AIAA Paper 95-0159, 1995.

[13]Engquist, B., and Majda, A., "Absorbing Boundary Conditions for the Numerical Simulation of Waves," *Mathematics of Computation*, Vol. 31, No. 139, 1977, pp. 629–651.

[14]Thompson, K. W., "Time-Dependent Boundary Conditions for Hyperbolic Systems, Part i," *Journal of Computational Physics*, Vol. 68, 1987, pp. 1–24.

[15]Thompson, K. W., "Time-Dependent Boundary Conditions for Hyperbolic Systems, Part ii," *Journal of Computational Physics*, Vol. 89, 1990, pp. 439–461.

[16]Atkins, H. L.,"Application of Essentially Non-Oscillatory Methods to Aeroacoustics Problems," *ICASE/LaRC Workshop on Benchmark Problems in Computational Aeroacoustics*, NASA CP 3300, 1994.

[17]Hu, F. Q., "On Absorbing Boundary Conditions for Linearized Euler Equations by a Perfectly Matched Layer," *Journal of Computational Physics*, Vol. 129, 1996, pp. 201–219.

[18]Hesthaven, J. S., "The Analysis and Construction of Perfectly Matched Layers for the Linearized Euler Equations," Inst. for Computer Applications in Science and Engineering, ICASE Rept. 97-49, 1997.

[19]Hardin, J. C., Ristorcelli, J. R., and Tam, C. W. (eds.), *ICASE/LaRC Workshop on Benchmark Problems in Computational Aeroacoustics*, NASA CP 3300, 1994.

[20]Meadows, K. R., Kumar, A., and Hussaini, M. Y., "A Computational Study on the Interaction Between a Vortex and a Shock Wave," AIAA Paper 89-1043, 1989.

[21]Ellzey, J. L., Henneke, M. R., Picone, J. M., and Oran, E. S., "The Interaction of a Shock with a Vortex: Shock Distortion and the Production of Acoustic Waves," *Physics of Fluids*, Vol. 7, 1995, pp. 172–184.

[22]Kao, C. T., von Ellenrieder, K., MacCormack, R., and Bershader, D., "Physical Analysis of the Two-Dimensional Compressible Vortex-Shock Interaction," AIAA Paper 96-0044, 1996.

[23]Jiang, G. S., and Shu, C. W., "Efficient Implementation of Weighted ENO Schemes," *Journal of Computational Physics*, Vol. 126, 1996, p. 202.

[24]Loh, C. Y., Hultgren, L. S., Chang, S.-C., and Jorgenson, P. C. E., "Vortex Dynamics Simulation in Aeroacoustics by the Space–Time Conservation Element and Solution Element Method," AIAA Paper 99-0359, 1999.

P. J. Morris
Associate Editor